Quasiperiodic Vibration of a Rotor in a Magnetic Bearing with Geometric Coupling

Murali Chinta*, Alan B. Palazzolo*, Albert Kascak**

* Department of Mechanical Engineering, Texas A&M University
College Station, Texas 77843-3123, USA
tel:+1-409-845-1836; fax:+1-409-845-3081; e-mail:chinta@tamu.edu

** U.S. Army @ NASA Lewis Research Center
Cleveland, Ohio 44135, USA
tel:+1-216-433-6024; fax:+1-216-433-5170

Abstract: This paper develops a one-dimensional model of the magnetic flux to estimate the magnetic forces by including the pole face curvature. Accounting for the pole face curvature results in a normal force that is perpendicular to the principal force; this causes geometric coupling of forces. The non-dimensional equations of motion are derived for a point mass rotor in one magnetic bearing with PD current feedback and geometric coupling. The steady-state nonlinear vibrations are then investigated. The rotor-bearing system has the softening spring type nonlinearity and exhibits characteristic jumps and hysteresis. When speed is increased, the presence of geometric coupling increases the rotor displacement before the jump and decreases the displacement beyond the jump. Geometric coupling also causes quasiperiodic vibration of the rotor. The (a)periodicity of the rotor motion is discussed using Poincaré maps and bifurcation diagrams. Increasing the differential gain of the controller could not damp the quasiperiodic motion to a periodic one.

List of Symbols

A	pole area, m^2
B_j	magnetic flux density of pole j, T
c	radial clearance, m
e	mass imbalance eccentricity, m
E	dimensionless eccentricity
F_B, F_L, F_R, F_T	forces of Bottom, ...magnets, N
$F_{BN},...$	non-dimensional magnetic forces
F_p, F_n	principal and normal forces, N
F_x, F_y	magnetic forces on rotor in X, Y, N
$\mathcal{F}$	magnetomotive force, ampere-turns
G_D	differential feedback gain, A/m/s
G_P	proportional feedback gain, A/m
G_{DN}, G_{PN}	non-dimensional feedback gains
h	pole width, m
H	magnetic field strength, A/m
I	current to electromagnet, A
I_{bias}	bias current, A
L	air gap, m
m	rotor mass, kg
n	dimensionless normal coordinate
N	number of winding turns
r_a	rotor radius, m
R	coil resistance, Ω
$\mathcal{R}$	gap reluctance, 1/H
t	time, s
x, y	rotor displacement coordinates, m
X, Y	dimensionless coordinates
α	geometric coupling coefficient
δ	term defined in Eq. 12
ϵ	dimensionless rotor displacement
Λ	term defined in Eq. 12
ζ	damping ratio
η	term defined in Eq. 5
θ_{uj}	angle from U-axis to pole j, rad
θ_{xu}	X to U counter-clockwise angle, rad
μ_0	permeability of free space, H/m
τ	dimensionless time
ω	rotor speed, rad/s
ω_n	linear natural frequency, rad/s
Ω	dimensionless rotor speed

1 Introduction

Active Magnetic Bearings(AMB) levitate a rotor by the attractive forces generated in a magnetic field due to the electromagnets. The AMB are electro-mechanical systems with their stiffness and damping properties dependent on both electronic and mechanical components. Thus the stiffness and damping of the rotor/bearing system can be controlled. The magnetic bearings also have several other advantages such as rotor speed being limited by the strength of the rotor material, low bearing losses, etc. [1]. Due to such features, the magnetic bearings are finding increasing number of applications in rotating machinery.

Gyroscopic effects cause Hopf bifurcation of rotor equilibrium position [2]. They use a nonlinear feedback control to stabilize the resulting unstable limit cycle. The nonlinear resonant frequencies were obtained for a rotor – magnetic bearing system with proportional control using the perturbation method of multiple scales [3].

The normal and attractive principal forces of electromagnets were experimentally determined in [4]. Their two-dimensional finite element model predicted the presence of normal forces. Including geometric coupling and using flux control results in multiple solutions at primary resonance of a point mass rotor [5]. They also obtained fractal boundaries separating stable and unstable regions in an eccentricity - rotor speed diagram and discussed the effects of other system parameters on these regions.

By allowing the air gap at a point on a pole to be a spatial function of rotor displacement and not constant over the entire pole area, this paper includes the poles' curvatures in estimating the magnetic forces. This is done by modifying a one-dimensional model of the magnetic flux using a "variable reluctance" approach. This results in the presence of normal forces, thus causing geometric coupling of forces. The results from this approach are then verified by comparing to those obtained from a two-dimensional finite element method and from experiments of [4].

The forces of a magnetic bearing with linear current control are nonlinear functions of rotor position and current. Thus the model used here is nonlinear despite the geometric coupling. This is different from the case when a flux control is used where the nonlinearity is only due to the geometric coupling as in [5]. Thus this paper studies the effects of geometric coupling on the steady-state response of a rotor in a magnetic bearing system with current control.

As this paper studies the rigid body vibrations, the assumption of co-location of sensors and magnetic bearing is suitable. When the flexible modes of vibration are to be considered, collocation becomes an important issue; see [6] and [7]. Some novel control strategies were used to minimize the vibration at resonance for a flexible mode in [8].

2 Rotor-Bearing Model

The AMB consists of four electromagnets placed symmetrically about the horizontal and vertical axes. PD Controller / Power Amplifier pairs are used in independent - axis control. A pair of identical displacement sensors measure the positive x and y displacements as shown in Fig. 1.

Current control is used in the feedback loop. The current input to each pole-pair is the sum of a bias current and a control current. The currents are input to the "left" and "right" pole-pairs in a "differential driving mode" as given below:

$$I_{L,R} = I_{bias} \pm (G_P\,x + G_D\,\dot{x}) \qquad (1)$$

where G_P and G_D are the controller's proportional and differential gains. This setup requires only one controller/amplifier pair per axis. Likewise, in the Y direction,

$$I_{B,T} = I_{bias} \pm (G_P\,y + G_D\,\dot{y}) \qquad (2)$$

2.1 Magnetic Forces

Ampere's law relating the magnetic field strength H and the current NI that causes it for an electromagnet is

$$\oint H.dl = NI \qquad (3)$$

Neglecting the reluctance of stator and rotor material in comparison to that of gap's, the above equation can be written as

$$2\mathcal{R}BA = NI \qquad (4)$$

where

$$A = \pi r_a h/6 \qquad \mathcal{R} = L/(\mu_0 A) \qquad B = \mu_0 H$$

r_a is rotor radius, h is pole width, and μ_0 is the permeability of free space.

The above equation implies that the reluctances of the two gaps of a magnet are the same. Including pole face curvatures into the model results in different gaps, reluctances for the two gaps. This is accomplished by modifying Eq. 4.

$$\mathcal{R}_1 BA = \eta NI, \quad \mathcal{R}_2 BA = (1-\eta)NI \qquad (5)$$

where

$$\eta = \mathcal{R}_1/(\mathcal{R}_1 + \mathcal{R}_2) \qquad (6)$$

The validity of such an approximation is verified by comparing the results with those available in literature: theoretical – two-dimensional finite element method, and experimental.

The following analysis considers pole curvatures, gap lengths, reluctances and flux densities to obtain the forces exerted by a magnetic pole on the rotor as functions of rotor position. X-Y is the globally fixed coordinate system whose origin is the bearing center O, U-V is the line-of-centers coordinate system whose origin is the rotor position (x,y). The angle from the X-axis to U-axis, θ_{xu}, is dependent on rotor position.

2.1.1 Gap length

Gap length for pole j at an angle θ_j from U-axis is given by

$$L_j = c - \sqrt{x^2 + y^2}\,cos\theta_j = c(1 + \epsilon\,cos\theta_j) \qquad (7)$$

where c is the magnetic bearing's radial clearance.

For a pole that subtends 30^0 at O, then, the lower and upper limits of θ_j are θ_{uj} and $\theta_{uj} + \pi/6$, respectively, where θ_{uj} is the angle from U-axis to the beginning of pole j in the counterclockwise direction.

2.1.2 Gap Reluctance

Gap reluctance for pole j, $\mathcal{R}_{gj}$, is given by:

$$\frac{1}{\mathcal{R}_{gj}} = \int \frac{\mu_0\,dA_j}{L_j} = \frac{\mu_0 r_a h}{c} \int \frac{d\theta_j}{1 + \epsilon\,cos\theta_j} \qquad (8)$$

2.1.3 Flux Density

The flux density for pole j is given by

$$B_j(\theta_j) = \frac{3\mathcal{F}_j \mu_0}{\pi c} \frac{1}{1 + \epsilon\,cos\theta_j} \qquad (9)$$

where $\mathcal{F}_j = \eta NI$, if j is odd, and $\mathcal{F}_j = (1-\eta)NI$, otherwise; $I = I_R$ for j=1,2, $I = I_T$ for j=3,4, etc.

2.1.4 Forces

The attractive force of a pole on the rotor has components in U and V directions:

$$F_{uj} = \int \frac{B_j^2(\theta_j)dA_j}{2\mu_0} \cos\theta_j$$

$$= \frac{\mathcal{F}_j{}^2 \mu_0 r_a h}{8c^2} \int \frac{\cos\theta_j}{(1+\epsilon\cos\theta_j)^2} d\theta_j \qquad (10)$$

and

$$F_{vj} = \frac{\mathcal{F}_j{}^2 \mu_0 r_a h}{8c^2} \int \frac{\sin\theta_j}{(1+\epsilon\cos\theta_j)^2} d\theta_j \qquad (11)$$

The integrals in the above expressions are evaluated in [9]:

$$\int \frac{d\theta_j}{1+\epsilon\cos\theta_j} = \frac{\delta}{\sqrt{1-\epsilon^2}} \cos^{-1}(\frac{\epsilon+\cos\theta_j}{1+\epsilon\cos\theta_j})$$

$$= \Lambda \qquad (12)$$

where $\delta = 1$ for $\sin\theta_j \geq 0$ and $\delta = -1$ for $\sin\theta_j < 0$.

$$\int \frac{\cos\theta_j}{(1+\epsilon\cos\theta_j)^2} d\theta_j = \frac{1}{1-\epsilon^2}(\frac{\sin\theta_j}{1+\epsilon\cos\theta_j} - \epsilon\Lambda) \quad (13)$$

$$\int \frac{\sin\theta_j}{(1+\epsilon\cos\theta_j)^2} d\theta_j = \begin{cases} \frac{1}{\epsilon(1+\epsilon\cos\theta_j)} & \text{if } \epsilon \neq 0 \\ -\cos\theta_j & \text{otherwise} \end{cases}$$
$$(14)$$

The forces in the X, Y directions are obtained by the coordinate transformation:

$$F_{xj} = F_{uj}\cos\theta_{ux} + F_{vj}\sin\theta_{ux} \qquad (15)$$
$$F_{yj} = -F_{uj}\sin\theta_{ux} + F_{vj}\cos\theta_{ux} \qquad (16)$$

The resultant force on the rotor due to the magnets has the components:

$$F_x = \sum_{j=1}^{8} F_{xj}, \qquad F_y = \sum_{j=1}^{8} F_{yj} \qquad (17)$$

2.2 Model Verification

For an electromagnet, the principal force is along the axis of symmetry of, and towards, the magnet. A normal force exists only if the rotor is offset from this axis of symmetry and it is in the direction of the offset and perpendicular to the principal force. To verify the accuracy of the present model, the normal force (X-direction) of the magnet in positive Y direction is estimated for the offset value $x/c = 0.45$ for several Y positions. Comparison to the two-dimensional finite element model results and experimental results given in [4] is shown in Fig. 2. In the figure, 'ktest' and 'kmodel' refer to the experimental and FEA results of [4], and 'this' refers to the model used in this paper. The present model compares well with the finite element model, and the differences are

perhaps because their model includes material B-H non-linearity also. Both the theoretical models, however, underestimate the normal force. The principal forces from the theoretical models agree well with the experimental results but are not presented here.

To use the higher geometric coupling values found from experiments, following [4], for a magnet the principal and normal forces are given by

$$F_p = \frac{B^2 A}{\mu_0} = \frac{\mu_0 A(NI)^2}{4L^2} \qquad (18)$$

$$F_n = \alpha n F_p \qquad (19)$$

where L is the constant gap for a pole-pair obtained from Eq. 7 with θ_j now being the angle between the U-axis and the appropriate principal axis; $n = x/c$ (if F_n is along X-axis), $n = y/c$ (otherwise); α is the geometric coupling coefficient which from experiments was reported to have an average value of 0.16.

The resultant magnetic force on the rotor has the components

$$F_x = F_R - F_L + \alpha(x/c)(F_T + F_B) \qquad (20)$$
$$F_y = F_T - F_B + \alpha(y/c)(F_R + F_L) \qquad (21)$$

2.3 Equations of Motion

For a rotor with a mass imbalance eccentricity of e and rotating in the counterclockwise direction the equations of motion are

$$m\ddot{x} = F_x + me\omega^2 \cos\omega t \qquad (22)$$
$$m\ddot{y} = F_y + me\omega^2 \sin\omega t \qquad (23)$$

Defining dimensionless variables as

$$X = x/c \qquad G_{PN} = cG_P/I_{bias}$$
$$Y = y/c \qquad G_{DN} = c\omega_n G_D/I_{bias}$$
$$E = e/c \qquad \Omega = \omega/\omega_n$$
$$\tau = \omega_n t$$

where the linear natural frequency is given by

$$\omega_n = \sqrt{\frac{\mu_0 A N^2 I_{bias}^2 G_{PN}}{mc^3}} \qquad (24)$$

The damping ratio is

$$\zeta = \frac{G_{DN}}{2G_{PN}} \qquad (25)$$

The dimensionless equations of motion are

$$X'' = F_{RN} - F_{LN} + \alpha X(F_{TN} + F_{BN}) + E\Omega^2 \cos\Omega\tau \qquad (26)$$

$$Y'' = F_{TN} - F_{BN} + \alpha Y(F_{RN} + F_{LN}) + E\Omega^2 \sin\Omega\tau \qquad (27)$$

where the primes are derivatives with respect to τ, and

$$F_{RN} = \frac{[\frac{1-(G_{PN}X+G_{DN}X')}{1-X}]^2}{4G_{PN}} \qquad (28)$$

$$F_{LN} = \frac{[\frac{1+(G_{PN}X+G_{DN}X')}{1+X}]^2}{4G_{PN}} \qquad (29)$$

$$F_{TN} = \frac{[\frac{1-(G_{PN}Y+G_{DN}Y')}{1-Y}]^2}{4G_{PN}} \qquad (30)$$

$$F_{BN} = \frac{[\frac{1+(G_{PN}Y+G_{DN}Y')}{1+Y}]^2}{4G_{PN}} \qquad (31)$$

Thus the parameters in the dimensionless equations are the stiffness term G_{PN}, damping term G_{DN}, rotor speed term Ω, eccentricity term E, and the geometric coupling coefficient α.

3 Analysis

In the following, various non-dimensional parameters are studied. Fig. 3 shows the stable Y-direction forces for various values of the stiffness term G_{PN} in the absence of geometric coupling. Clearly for a positive Y displacement, a stable restoring force in the Y-direction has to be negative. For a given value of Y, the larger the value of G_{PN} the larger is the restoring force. The figure also shows that with increasing G_{PN} the maximum possible value of F_y decreases and the peak values occur at lower values of Y.

To obtain the rotor motion, the equations were numerically integrated using the fourth-order Runge-Kutta method. Fig. 4 shows the frequency response curve in the absence of geometric coupling. It shows the softening spring characteristic, jumps and the hysteresis region of this nonlinear rotor-bearing system. As numerical integration is used, only stable solutions are obtained.

Figure 5 shows the frequency response curve for the geometric coupling coefficient $\alpha=0.16$. With increase in speed, the effect of α is to reduce the stiffness before the jump and increase it beyond the jump. Beyond resonance, as the presence of geometric coupling decreases the rotor displacement, higher values of α can provide stable rotor operation for higher eccentricities. This is verified in Fig. 6.

As examining the subharmonic motion is of interest here, 'Poincaré maps' and 'bifurcation diagrams' are useful tools for the purpose. These tools give no information on the superharmonic content of rotor motion. A simple Poincaré map can be obtained by sampling the rotor orbit once every rotor revolution at some phase. A Poincaré map with n discrete points represents a Period-n rotor motion i.e. the lowest frequency is 1/n times the rotor speed. A bifurcation diagram gives the qualitative changes in the dynamics when a parameter of the rotor-dynamic system is varied. It gives the Poincaré points for several values of a parameter such as eccentricity E.

The motion is Period-1 for $\alpha = 0.16$ for reasonable damping values. Fig. 7 shows the bifurcation diagram for the parameters $\alpha = 0.24$, $G_{PN} = 1.1$, $G_{DN} = 0.11$, $\Omega = 1$. For this set of parameters, the rotor motion is Period-1 for $E < 0.32$. For $E = 0.32 - 0.35$, the rotor motion has a large "subharmonic" content. The Poincaré maps, shown in Fig. 8, reveal that the motion is quasiperiodic as the Poincaré points lie on closed curves. The rotor steady-state motion changes qualitatively from periodic to quasiperiodic through a Hopf bifurcation which generates the frequency of amplitude modulation [10]. The resulting time series is shown in Fig. 9 and a corresponding phase-plane diagram in Fig. 10.

Increasing G_{DN} reduced the amplitude of periodic motion, as can be seen in Fig. 11 at $E = 0.45$. No qualitative change in the dynamics were seen for the parameter(E) range where quasiperiodic motion was seen for $G_{DN}=0.11$. However, the rotor has aperiodic motion for a wider range of values of E when G_{DN} is increased. When G_{DN} is decreased, the aperiodic motion is still present, though for a smaller range of values of E. So, to reduce the quasiperiodic motion to a periodic one, changing G_{DN} alone is insufficient.

4 Conclusions

In this paper it is demonstrated that pole curvature results in geometric coupling of forces. For a current control system, geometric coupling reduces the stiffness before the jump, when the speed is increased, and increases the stiffness beyond the jump. When the stiffness is small, geometric coupling causes quasiperiodic rotor motion which could not be damped to a periodic motion by increasing the controller's differential gain.

References

[1] G. Schweitzer, H. Bleuler and A. Traxler, "Active Magnetic Bearings: Basics, Properties and Applications," vdf Hochschulverlag AG an der ETH Zurich, 1994.

[2] A. M. Mohamad and F. P. Emad, "Nonlinear Oscillations in Magnetic Bearing Systems," IEEE Trans. on Automatic Control, Vol. 38, No. 8, pp. 1242-1245, 1993.

[3] C. Nataraj, "Nonlinear Analysis of a Rigid Rotor on Magnetic Bearings," ASME/IGTI Congress, Houston, Texas, 95-GT-204, 1995.

[4] J. D. Knight, Z. Xia and E. B. McCaul, "Forces in Magnetic Journal Bearings: Nonlinear Computation and Experimental Measurement," Proc. of Third International Symposium on Magnetic Bearings, Alexandria, Virginia, USA, pp. 441-450, 1992.

[5] L. Virgin, T. F. Walsh and J. D. Knight, "Nonlinear Behavior of a Magnetic Bearing System," ASME Journal of Engineering for Gas Turbines and Power, Vol. 117, No. 3, pp. 582-588, 1995.

[6] K. Nonami, T. Yamanaka and M. Tominaga, "Vibration and Control of a Flexible Rotor Supported by Magnetic Bearings," JSME International Journal, Series 3, Vol. 33, No. 4, pp.475-482, 1990.

[7] C. R. Burrows, P. S. Keogh and R. Tasaltin, "Closed-loop Vibration Control of Flexible Rotors - An Experimental Study," Proc. of IMechE, Part C: Journal of Mechanical Engineering Science, Vol. 207, pp. 1-17, 1993.

[8] O. Matsushita, N. Takahashi, M. Yoneyama and Y. Fukushima, "Unbalance Resonance Vibration Control for Magnetically Borne Flexible Rotors," IFTOMM, pp. 363-370, 1994.

[9] W. A. Gross, editor, "Fluid Film Lubrication," John Wiley & Sons, New York, 1980.

[10] J. M. T. Thompson and H. B. Stewart, "Nonlinear Dynamics and Chaos," John Wiley & Sons Ltd, Chichester, UK, 1988.
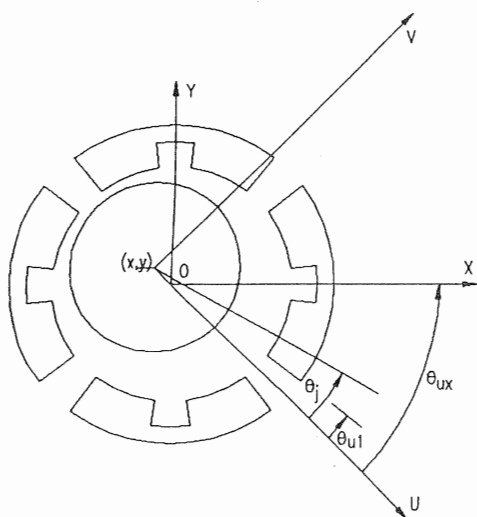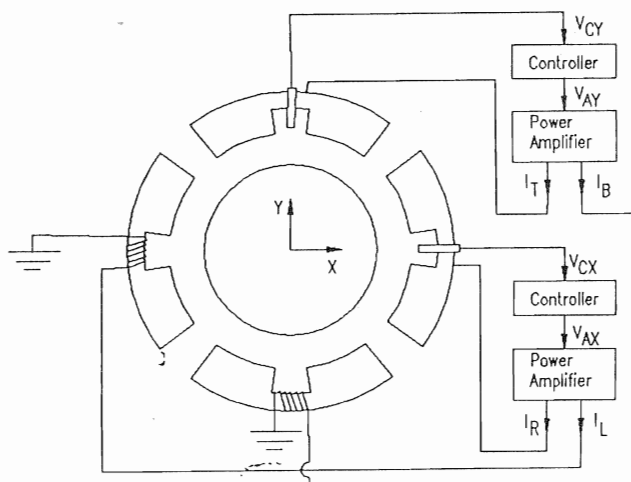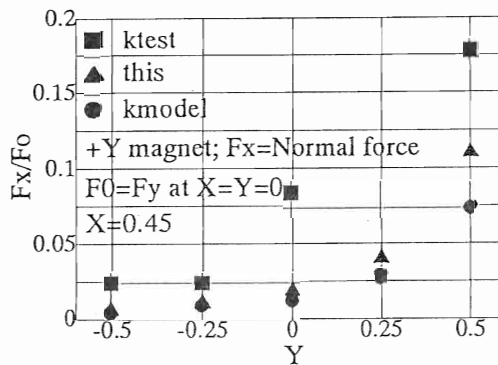
Fig. 1: Rotor-Bearing Model
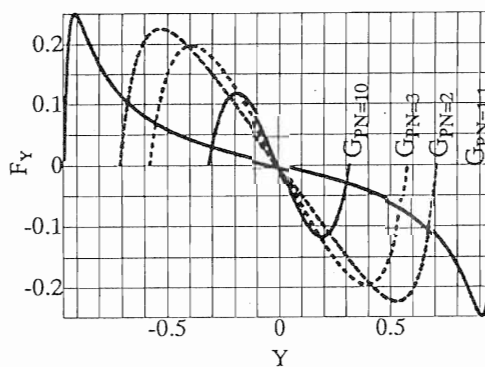

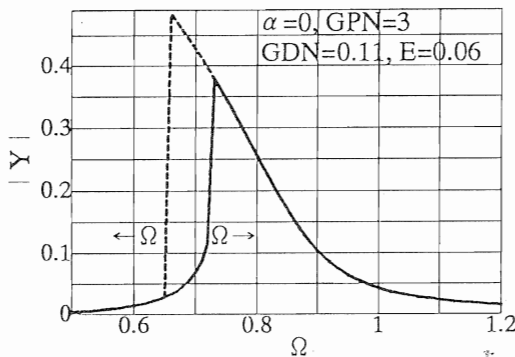
Fig. 2: Model Validation
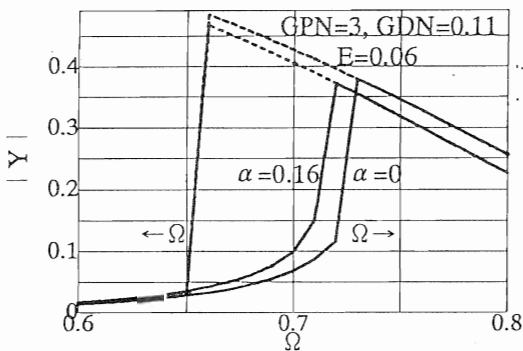

Fig. 3: Magnetic Force

Fig. 4: Frequency Response
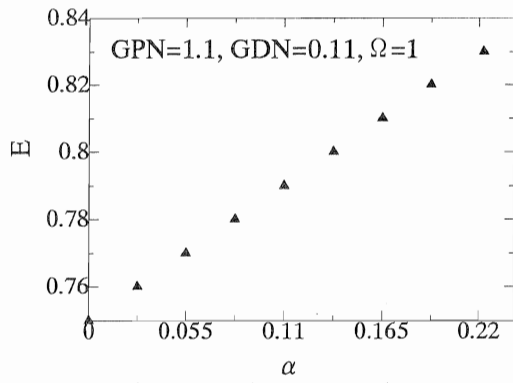

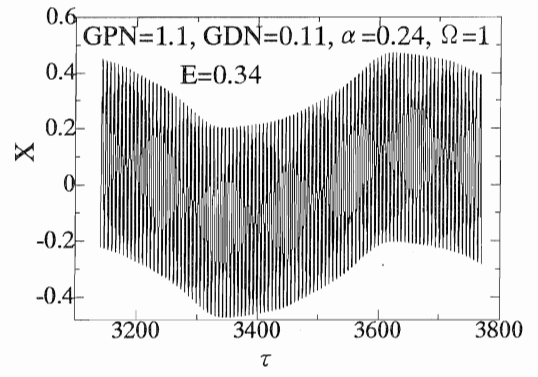Fig. 5: Frequency Response; vary α

Fig. 6: Maximum Unbalance

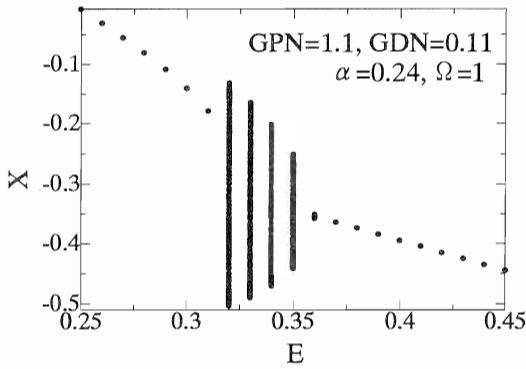Fig. 9: Amplitude-Modulated Response
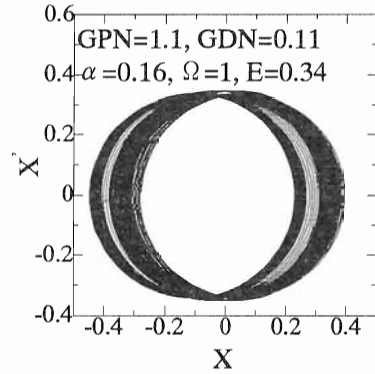

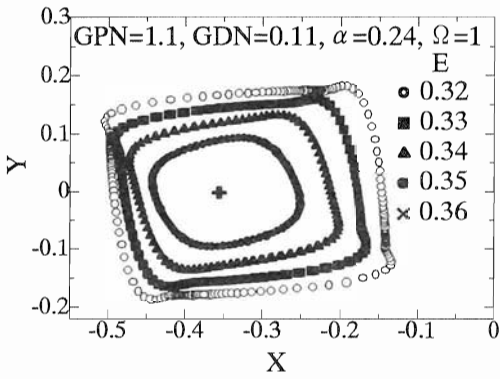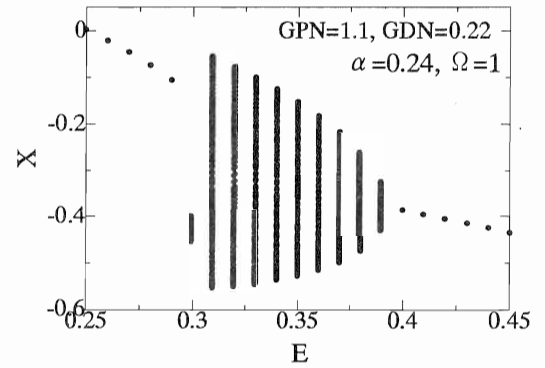Fig. 7: Bifurcation Diagram 1

Fig. 10: Phase-Plane Diagram

Fig. 8: Poincare Maps

Fig. 11: Bifurcation Diagram 2